Bending failure of a concrete gravity dam subjected to underwater explosion[*]

Xie-ping HUANG[†1], Jing HU[†‡2], Xue-dong ZHANG[2], Zi-tao ZHANG[2], Xiang-zhen KONG[3]

[1]Institute of Geotechnical Engineering, Zhejiang University, Hangzhou 310058, China
[2]China Institute of Water Resources and Hydropower Research, Beijing 100048, China
[3]Army Engineering University of PLA, Nanjing 210007, China
[†]E-mail: huangxieping@zju.edu.cn; jinghu@buaa.edu.cn
Received Apr. 29, 2020; Revision accepted July 11, 2020; Crosschecked Nov. 30, 2020

Abstract: Dam structures are prime targets during wars, and a tragedy is likely to happen in a populated area downstream of a dam exposed to explosions. However, experimental investigations of the failure of a concrete gravity dam subjected to underwater explosion (UNDEX) are extremely scarce. In this study, centrifuge tests and numerical simulations were performed to investigate the failure of a concrete gravity dam subjected to a near-field UNDEX. The results revealed the existence of two tensile fractures inside the dam, one in the upper part and the other in the lower part. Due to the narrowness of the upper part, there were coupled effects of bending tensile loads in the upstream face and a reflected tensile stress wave in the downstream face, resulting in severe tensile damage to the upper part in both the upstream and downstream faces. The fracture in the lower part was measured at around one third of the height of the dam. This fracture was produced mainly by the bending tensile loads in the upstream face. Driven by those loads, this fracture started from the upstream face and developed towards the downstream face, with a horizontal angle of about 15°. The underlying mechanisms behind the two tensile fractures were confirmed by recorded strain histories. The dam failures presented in this study are similar to those produced in historical wars, in which dams were under similar attack scenarios.

Key words: Centrifuge test; Numerical simulation; Concrete gravity dam; Underwater explosion (UNDEX); Bending failure
https://doi.org/10.1631/jzus.A2000194   **CLC number:** TV642.3

1 Introduction

Dam structures are societal facilities usually used for storage of water and generation of electricity. Owing to their significant political and economic benefits, dam structures are likely targets for terrorist attack scenarios and wars. A tragedy in the downstream area is likely to happen if a dam with a lot of water in its reservoir is exposed to blasts. Previous studies (Cole and Weller, 1948; Rajendran and Lee, 2009) have revealed that an underwater explosion (UNDEX) causes significantly more severe damage to structures than an air blast with the same mass of explosives. Concrete gravity dams are one of the most common types of dams. Extensive attention, therefore, has been drawn to the failures of a concrete gravity dam subjected to UNDEX. However, field tests require the use of relatively large amounts of charges, which involves potential risks. Thus, they are typically not feasible in civilian research. Besides, full-scale tests are often unaffordable. The physical process includes the explosion, the shock wave propagation in fluids, fluid–structure interactions, and the response of dam structures. It is extremely difficult to investigate this subject completely by theory.

Therefore, studies related to this topic have been based mainly on small-scale tests (Vanadit-Ellis and Davis, 2010; Lu et al., 2014) and numerical simulations (Wang and Zhang, 2014; Zhang et al., 2014; Lu et al., 2016; Chen et al., 2017; Li et al., 2018; Saadatfar and Zahmatkesh, 2018; Yang et al., 2018; Kalateh, 2019; Ren and Shao, 2019).

Hammer impact methods were used by Lu et al. (2014) in model tests to study the influence of a strong underwater shock wave on a high concrete dam. Six 1:200 scale model tests were carried out. The test results revealed that impact failure started with a fracture on the top of the dam followed by another in the dam body. However, the hammer impact method can generate only a plane shock wave, which is far from a realistic spherical shock wave induced by UNDEX. The difference is evident, especially for a near-field UNDEX. Besides, this kind of small-scale model test is unable to reproduce the internal state of stresses of a dam prototype caused by the great mass of the dam and the hydrostatic pressure of the reservoir. Therefore, realistic damage and failure of dam structures cannot be expected. Recently, with the continuous development of centrifuge apparatus and similarity theory (Hu et al., 2017, 2020b), researchers have been able to investigate this topic using a centrifuge, which can completely reproduce the gravity-field of a prototype dam. A 1:100 scale model of a typical gravity dam in a centrifuge was designed by Vanadit-Ellis and Davis (2010). With this model, a series of centrifuge tests were performed to investigate the response of a dam subjected to UNDEX. The test results revealed three typical damage modes, namely, (1) localized damage in the form of cratering or radial cracks normal to the upstream face; (2) tensile splitting or shearing failures; (3) bending failures (vertical or horizontal cracks normal to the upstream face). This kind of work is rare and valuable. However, the detailed configurations of the centrifuge tests were not presented, including the mass of the explosives, the position of the explosions, and the water depth, which play major roles in the damage and failure of dams (Wang and Zhang, 2014; Zhang et al., 2014; Chen et al., 2017; Saadatfar and Zahmatkesh, 2018). This creates difficulties for other researchers attempting to carry out comparative analyses. More experimental studies related to this topic are needed.

With the rapid development of computer technology and the advancement of numerical methods, it has become easy and feasible to investigate the response of dams subjected to UNDEX through computer simulation. Numerous numerical studies (Xu et al., 2013; Wang and Zhang, 2014; Zhang et al., 2014; Lu et al., 2016; Chen et al., 2017; Li et al., 2018; Saadatfar and Zahmatkesh, 2018; Yang et al., 2018; Kalateh, 2019; Ren and Shao, 2019) are available. Coupled Euler–Lagrange finite element method was established by Kalateh (2019) to analyze the failure of concrete dams under blast loadings. Yang et al. (2018) used a smoothed particle hydrodynamics (SPH)–Lagrangian–Eulerian approach for the simulation of concrete gravity dams subjected to the combined effects of penetration and explosion. Li et al. (2018) studied the influence of hydrostatic pressure on a concrete gravity dam subjected to UNDEX. Furthermore, many numerical studies (Wang and Zhang, 2014; Zhang et al., 2014; Chen et al., 2017; Saadatfar and Zahmatkesh, 2018) have focused on the effects of the explosion positions (standoff distance, detonation depth), the weight of the charge, and the water depth. However, a comparative analysis with small-scale tests was lacking in most except the following studies. Lu et al. (2016) compared numerical simulations and small-scale tests (Lu et al., 2014), and obtained a good agreement. Based on the centrifuge test results obtained by Vanadit-Ellis and Davis (2010), Ren and Shao (2019) performed numerical studies, and the results confirmed the reproducibility of the three failure modes observed by Vanadit-Ellis and Davis (2010). More numerical studies supported by test results are still needed.

The purpose of this study was to carry out a comparative investigation of the failures of a concrete gravity dam subjected to near-field UNDEX as revealed by a centrifuge test and numerical simulations. The detailed configurations of the centrifuge test are given to enable other researchers to validate their numerical models. The underlying mechanism behind the observed dam failures was carefully verified.

2 Materials and methods

The model setups and the materials used in the centrifuge tests and numerical simulations are

presented in this section. To perform a comparative study, the model setup of the numerical simulations was installed based on the centrifuge tests, with identical dam geometry and similar boundary conditions. The required material parameters for numerical simulations were also derived based on the concrete specimens used in the centrifuge tests. The precise TNT (trinitrotoluene) equivalent of the industrial detonator used in the centrifuge tests was calibrated using the recorded information of the shock wave and gas bubble produced by UNDEX. The calibrated TNT equivalent was then adopted in the numerical simulations.

2.1 Centrifuge tests

2.1.1 Centrifuge model setup

The centrifuge at the Institute of Water Resources and Hydropower Research (IWHR), China was used in this study. This centrifuge provides a maximum centrifugal acceleration of 300g (g is the acceleration of gravity) with a maximum rotation radius of 5.03 m and a payload of 150 t. The dam model was placed in an aluminum alloy container, which was accelerated by a centrifuge. The technique for conducting underwater explosion tests in a centrifuge was introduced by Hu et al. (2020a). To simulate the true dynamic response of each dam block under UNDEX, the dam model was composed of three identical dam blocks. The dam body and foundation of each dam block were poured with cement mortar as a whole. The interfaces between the dam blocks and those between the dam and container were treated to retain water. Fig. 1 shows the concrete dam model and its installation. The geometric dimensions of the dam block are shown in Fig. 2.

Several strain gauges were installed on the downstream surface of the middle dam block. The strain gauges were a resistance type and each had a resistance of (120.1±0.2) Ω, with a sensitivity index φ=(2.08±1)%. A 1/4 Wheatstone bridge was used to measure the strain. PCB-138A10 pressure sensors, with a range of 0–68 MPa, a resonant frequency larger than 1000 kHz, and a rise time lower than 1.5 μs were used for shock wave pressure measurements. In the tests, these pressure sensors were placed at the same altitude as the center of the explosive. Generally, two pressure sensors at different positions were used in each test.
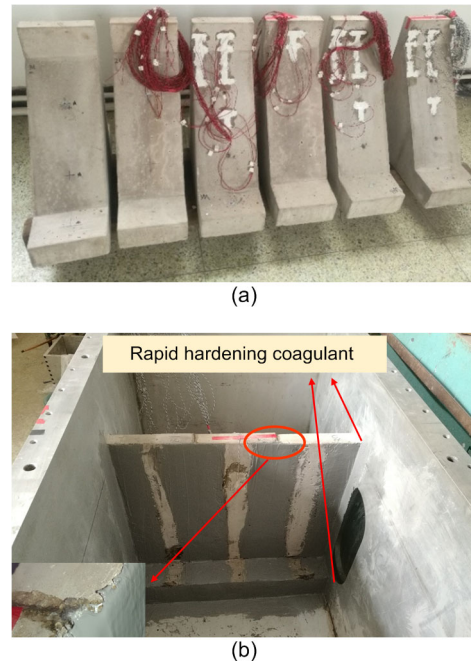

(a)

(b)

Fig. 1 Concrete dam model of centrifuge tests: (a) dam model; (b) model installation
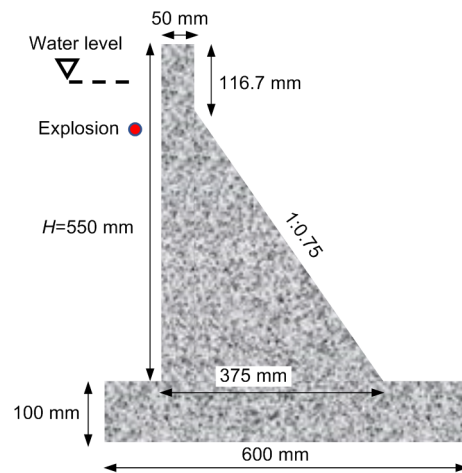

Fig. 2 Dam geometry

The concrete dam was prefabricated with cement mortar. The cement mortar of 1 m³ was composed of 255-kg water, 235-kg cement, 157-kg limestone powder, and 1647-kg sand. The compressive strength and tensile strength (Table 1) were obtained for each batch of the specimens by standard compressive and tensile tests, respectively. Table 2 shows four representative UNDEX tests (UE-01 to UE-04) in a centrifuge, organized as combinations of variable centrifugal accelerations and positions of the detonator. UE-01, UE-02, and UE-03 were arranged to check the

data acquisition system and calibrate the TNT equivalent of the industrial detonator. UE-04 was arranged to investigate the failure of a concrete gravity dam.

Table 1 Parameters of the cement mortar

Specimen number	Mass (in 1-m³ cement mortar) (kg)			
	Water	Cement	Limestone	Sand
YT-1	255	235	157	1647

Specimen number	Compressive strength (MPa)		Tensile strength (MPa)
	7 d	28 d	
YT-1	10.3	14.9	1.46

Values 7 d and 28 d denote the curing times of cement mortar

Table 2 Centrifuge test scheme

Parameter	Description			
	UE-01	UE-02	UE-03	UE-04
n (×g)	50	50	20	80
Detonator number	1	1	1	2
H_w (mm)	600	500	600	600
L (mm)	300	200	300	100
R_c (mm)	–	–	–	20
P_1 (mm)	250	185	185	300
P_2 (mm)	–	245	250	380
Specimen	–	–	–	YT-1

n denotes the centrifugal acceleration; H_w represents the water depth, measured from the foundation bottom to the water level; L denotes the detonation depth measured from the explosion center to the water level; R_c represents the standoff distance measured from the explosion center to the upstream face; P_1 and P_2 represent the distances from the pressure sensors to the explosion center

2.1.2 TNT equivalent calibration

An industrial detonator was used in the centrifuge tests. The precise TNT equivalent of the detonator was unknown and thus the detonator needed to be calibrated using test data. Generally, the TNT equivalent of a detonator can be calibrated individually by the energy of the gas bubble and shock wave generated by UNDEX. The widely accepted parameters for TNT explosive defined by Swisdak Jr (1978) were adopted as a reference (Table 3). The energy of the gas bubble, E_b, was derived from the Cole and Weller theory (Cole and Weller, 1948), by the following equation:

$$E_b = 0.684W \rho_w g^{5/2} K_T^3, \qquad (1)$$

where W is the mass of TNT explosive, ρ_w is the

density of water, and K_T is the slope coefficient in Eq. (2) (Snay, 1962; Snay and Tipton, 1963):

$$T_b = K_T W^{1/3} / (H_0 + H_w)^{5/6}, \qquad (2)$$

where T_b represents the period of the gas bubble, $H_0 = P_0/\gamma_w$ is the equivalent water depth of the atmospheric pressure, with P_0 being the atmospheric pressure and γ_w being the product of ρ_w and g. By assuming the TNT equivalent of a detonator is 1.0 g, the T_b–$W^{1/3}/(H_0+H_w)^{5/6}$ curve was obtained (Fig. 3). A linear relationship was observed with a slope coefficient of 2.17336. According to Eq. (1) and the parameters for TNT explosive listed in Table 3, the energy of the detonator E_d could be obtained by $E_d/E_b=(2.17336/2.11)^3=1.093$. Thus, the precise TNT equivalent of the detonator was calibrated as 1.093 g.

Table 3 Calibrated parameters of the industrial detonator

Explosive type	Density (kg/m³)	K_T	K_E	α_E	K_p	α_p
TNT explosive	1600	2.11	84.40	2.04	52.5	1.13
Detonator in this study	1600 (assumed)	2.17	91.94	2.04	53.2	1.13

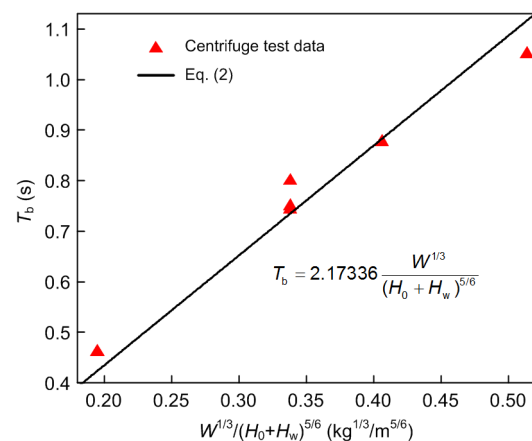K_E, α_E, K_p, and α_p are coefficients in Eqs. (5) and (6)

Fig. 3 Period of the gas bubble derived from the test data and Eq. (2)

The precise TNT equivalent of a detonator could also be calibrated by the energy of the shock wave. The energy of the shock wave E_s was obtained from the integral of the corresponding shock wave, based on the equation proposed by Cole and Weller (1948):

$$E_s = \frac{1}{\rho_w C_w} \int_0^{6.7\theta} P^2(t)\mathrm{d}t, \qquad (3)$$

where C_w is the sound velocity in water, θ is the time constant of the shock wave, and $P(t)$ is the pressure–time history of the shock wave, which is expressed as (Cole and Weller, 1948)

$$P(t) = P_m \mathrm{e}^{-t/\theta}, \qquad (4)$$

where P_m is the maximum pressure of the shock wave, which is determined by (Cole and Weller, 1948)

$$P_m = K_p \left(\frac{\sqrt[3]{W}}{R} \right)^{\alpha_p}, \qquad (5)$$

where R is the distance from the pressure sensor to the explosion center. In addition, the energy of the shock wave E_s could also be approximated by the following empirical formula (Cole and Weller, 1948):

$$E_s = K_E W^{1/3} \left(\frac{W^{1/3}}{R} \right)^{\alpha_E}. \qquad (6)$$

However, for an UNDEX in a centrifuge, the shock wave will inevitably be affected by the wall of the dam structures and the container. This is reflected in the existence of several peaks in the shock wave pressure–time histories (Fig. 4). Fig. 4 also shows the pressure–time histories predicted from Eq. (4) from Cole and Weller (1948). For this case, to obtain the realistic energy of the shock wave through Eq. (3), the contributions caused by the reflecting wave should be removed.

By assuming the TNT equivalent of the detonator was 1.0 g, the $E_b/W^{1/3}$–$W^{1/3}/R$ curve was obtained (Fig. 5). The exponent coefficient α_E was intentionally equal to that of TNT listed in Table 3, and the
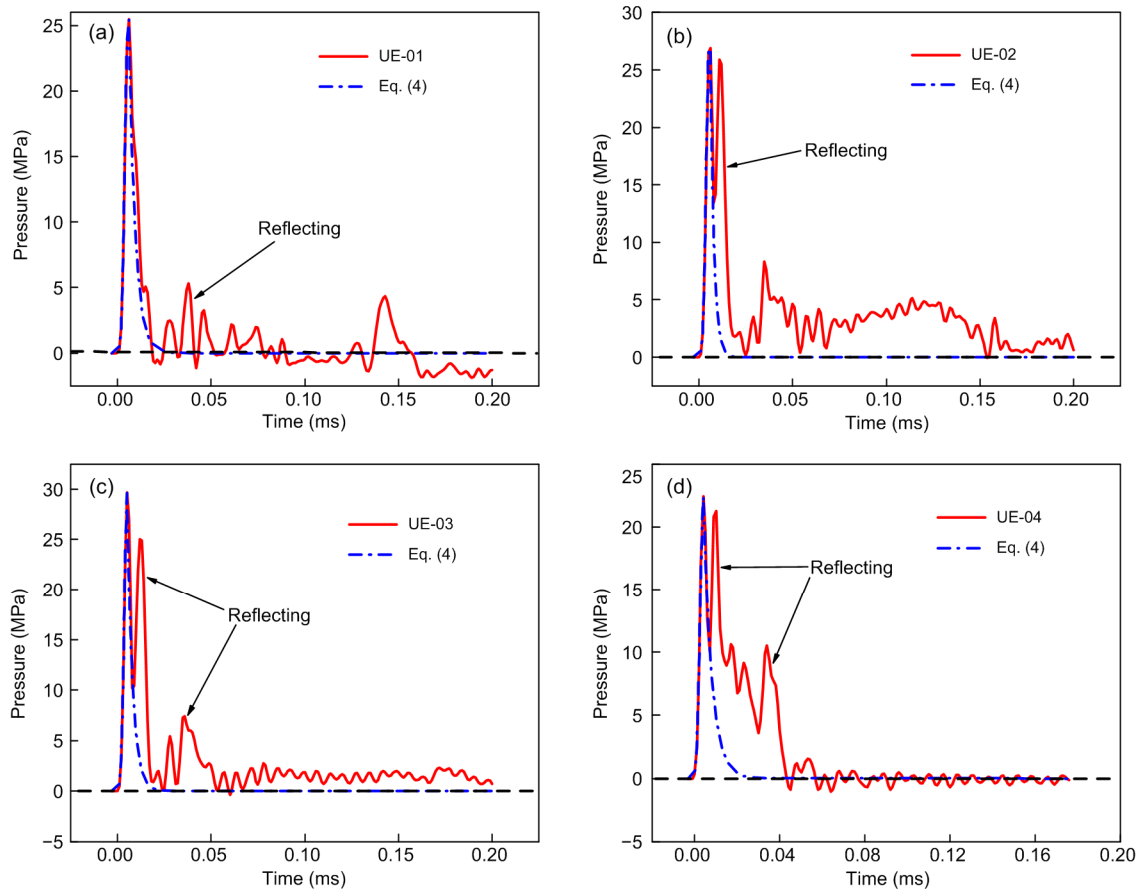

Fig. 4 Shock wave pressure–time histories derived from centrifuge test data and Eq. (4): (a) UE-01; (b) UE-02; (c) UE-03; (d) UE-04

slope coefficient K_E was calibrated as 91.94. According to Eq. (6) and Table 3, the energy of the detonator E_d could be obtained from E_d/E_s= 91.94/84.40=1.089. Thus, the precise TNT equivalent of the detonator was calibrated as 1.089 g, which is close to the 1.093 g obtained above through the energy of the gas bubble. The TNT equivalent of the detonator, E_d=$(E_d/E_b+E_d/E_s)/2$≈1.09 g, therefore, is used hereafter. Fig. 6 shows the P_m–$W^{1/3}/R$ curve. The coefficient K_p of this curve was determined as 53.2, which is quite close to 52.5 for TNT (Table 3).
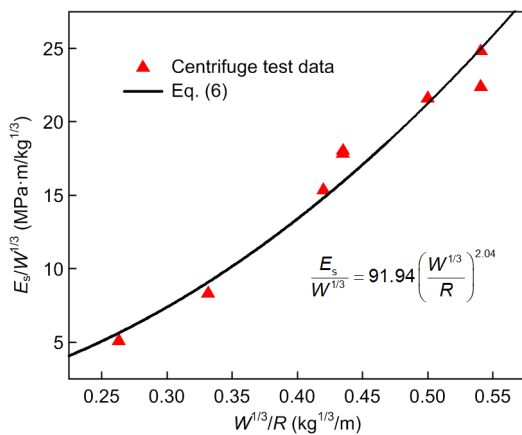

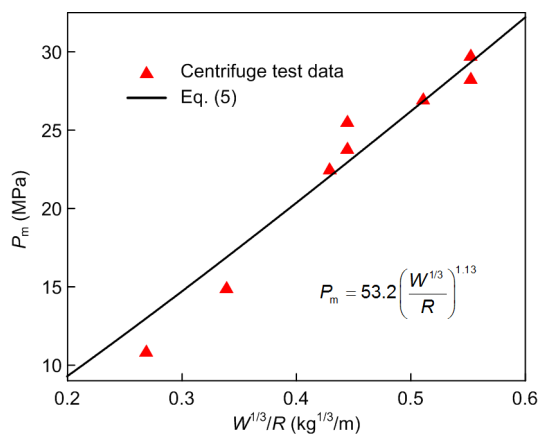**Fig. 5 Energy of the shock wave derived from centrifuge test data and Eq. (6)**

Fig. 6 Peak pressure of the shock wave derived from centrifuge test data and Eq. (5)

2.2 Numerical simulations

2.2.1 Numerical model setup

Fig. 7 illustrates the setup of the numerical model. The dam and the foundation were modeled as a whole, with geometric dimensions identical to those shown in Fig. 2. Considering the symmetry of the model, half of the dam, foundation, water, air, and explosive were modeled to reduce the computational cost. A coupled Lagrangian–Eulerian method was used (Benson, 1992). This method combines the advantages of Lagrangian and Eulerian meshes, which is useful for dealing with problems involving fluid–structure interactions. Lagrangian mesh was used for the dam and the foundation, with a mesh size of 3.5 mm. Eulerian mesh was adopted for the water, air, and explosive, with a mesh size of 4 mm. Based on the configuration of the centrifuge test UE-04, the arrangement of the numerical simulation was as follows. An acceleration of 80g was added vertically to the numerical model to simulate the centrifugal acceleration. A spherical explosive charge of 2.18 g TNT was used, based on the calibrated TNT equivalent of the industrial detonator. The standoff distance R_c was 20 mm, measured from the upstream face of the dam. The detonation depth L was 100 mm and the water depth H_w was 600 mm. Symmetric boundary conditions were applied to the symmetric plane. Along the truncated boundaries of the entire computational domain, the outflow boundary conditions were applied for the Eulerian mesh.
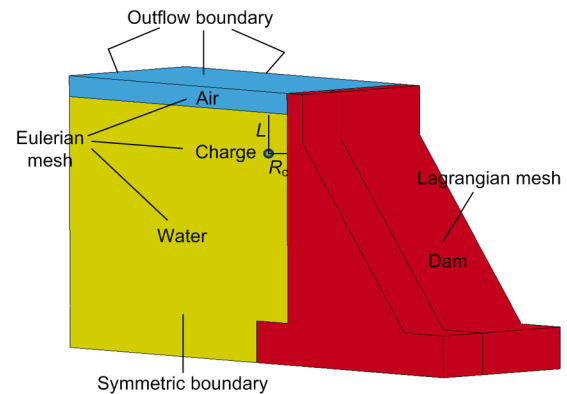

Fig. 7 Numerical model of a concrete gravity dam subjected to UNDEX

2.2.2 Constitutive model for concrete

The response of dam structures subjected to UNDEX is a complex, nonlinear, and rate-dependent process. The strength of the concrete material could be enhanced several times with a high-strain-rate loading process, as supported by many experimental

studies (Cadoni et al., 2000; Schuler et al., 2006; Yan and Lin, 2006; Huang et al., 2020c). Thus, a constitutive model capable of capturing the dynamic response of concrete structures under a high strain rate and high pressure should be selected. In this study, the model proposed by Kong et al. (2018) was adopted. An introduction to this model is presented as follows.

Two independent strength surfaces of compressive meridians, i.e. the maximum strength surface σ_m and the residual strength surface σ_r, were used in the model proposed by Kong et al. (2018), i.e.

$$\sigma_m = \begin{cases} 3\left[P/(1-D_{tol})+T\right], & P \leq 0, \\ 1.5(P+T)/\psi, & 0 < P \leq f_c/3, \\ f_c + \dfrac{P-f_c/3}{a_1+a_2P}, & P > f_c/3, \end{cases} \quad (7)$$

$$\sigma_r = \frac{P}{a_1+a_2P}, \quad (8)$$

where a_1 and a_2 are constants determined from a suitable set of triaxial compression data, f_c and T denote the unconfined uniaxial compressive strength and tensile strength, respectively, P represents the hydrostatic pressure, and D_{tol} is the total damage, as defined below. ψ denotes the tensile-to-compressive meridian ratio. The current failure surface $Y(\sigma_{ij}, D_{tol})$, as a function of the stress tensor σ_{ij} and total damage D_{tol}, was determined by interpolation between the maximum strength surface and the residual strength surface as follows:

$$Y(\sigma_{ij}, D_{tol}) = \sqrt{3J_2} = r'\left[D_{tol}(\sigma_r - \sigma_m) + \sigma_m\right], \quad (9)$$

where J_2 is the second deviatoric stress invariant, and r' denotes the ratio of the current meridian to the compressive meridian. To account for the strain rate effect, the current failure surface was enhanced by the "radial enhancement" approach, as follows (Hartmann et al., 2010):

$$Y = r_f Y(P/r_f), \quad (10)$$

where r_f denotes the dynamic increase factor (DIF), which was defined separately for compression and tension as follows (Xu and Wen, 2013), since experimental data showed that DIF for tension is much higher than that for compression:

$$\mathrm{DIF}_t = \left\{\tanh\left[\left(\log(\dot{\varepsilon}/\dot{\varepsilon}_0)-W_x\right)S\right](F_m/W_y-1)+1\right\}W_y,$$
$$\mathrm{DIF}_c = (\mathrm{DIF}_t-1)(T/f_c)+1, \quad (11)$$

where DIF_t and DIF_c represent the dynamic increase factors for tension and compression, respectively, $\dot{\varepsilon}$ is the strain rate, and $\dot{\varepsilon}_0 = 1$ s^{-1} represents the reference strain rate. $F_m=10$, $W_x=1.6$, $S=0.8$, and $W_y=5.5$ are fitting constants.

The tensile damage D_t is proposed as

$$D_t = 1-\left[1+\left(c_1\frac{\lambda}{\varepsilon_{frac}}\right)^3\right]\exp\left(-c_2\frac{\lambda}{\varepsilon_{frac}}\right) + \frac{\lambda}{\varepsilon_{frac}}(1+c_1^3)\exp(-c_2), \quad (12)$$

where ε_{frac} is the fracture strain, and $c_1=3$ and $c_2=6.93$ are constants. λ denotes a modified equivalent plastic strain defined as

$$\lambda = \begin{cases} \sum \dfrac{\Delta\bar{\varepsilon}_p}{d_1\left(T/f_c + P/f_c\right)^{d_2}}, & P > 0, \\ \sum \Delta\bar{\varepsilon}_1, & P \leq 0, \end{cases} \quad (13)$$

where $\Delta\bar{\varepsilon}_p$ is the effective plastic strain increment, d_1 and d_2 represent the damage constants, and $\Delta\bar{\varepsilon}_1$ is the plastic strain increment in the unconfined uniaxial tension (UUT) test, which is a function of $\Delta\bar{\varepsilon}_p$. The compressive damage D_c is proposed as

$$D_c = \frac{\tau\lambda}{\lambda+1}, \quad (14)$$

where τ is a constant that governs the strain softening stage. Then the total damage is determined by

$$D_{tol} = 1-(1-D_c)(1-D_t). \quad (15)$$

In the model of Kong et al. (2018), the tensile damage D_t and compressive damage D_c are defined and calculated separately, as functions of the modified equivalent plastic strain λ for tension and compression, respectively. Then, the total damage is

defined as a combination of the tensile damage and compressive damage, to consider the interactions between them. For instance, consider a concrete structure that first undergoes compression with compressive damage D_c=0.5, then suffers from tension with tensile damage D_t=0.5. The total damage to the concrete structure, according to Eq. (15), is 0.75 higher than 0.5. This indicates that the previous compressive damage, accompanied by degradation of the strength and stiffness of the concrete structure, acts on and weakens the tensile strength of the concrete when a subsequent tensile load is applied.

The interactions between tensile damage and compressive damage should be considered, especially in the case of cyclic loadings, where the loading scheme is typically compression–tension–compression. However, in the case of a concrete gravity dam under UNDEX, as in this study, tensile damage is dominant (as discussed in Section 3), which implies that the total damage D_{tol} degrades to the tensile damage D_t. In this context, D_{tol}=1, namely D_t=1 is typically accompanied by a tensile crack with D_c approaching or equaling zero.

The tabulated compaction equation of state (EOS) (EOS #8) in LS-DYNA (Hallquist, 2006) is used in the model, which gives the current pressure P as a function of the volumetric strain μ:

$$P = C_P(\mu) + \gamma_0 \theta_t(\mu) E_0, \quad (16)$$

where E_0 denotes the internal energy per unit initial volume, and γ_0 denotes the ratio of specific heat. $C_P(\mu)$ and $\theta_t(\mu)$ are the tabulated pressure and temperature as functions of the volumetric strain, respectively. The required parameters of the concrete dam for the model of Kong et al. (2018) are summarized in Table 4. The compressive and tensile strengths determined by standard compressive and tensile tests for the specimens of the centrifuge test UE-04 were adopted here. The remaining parameters were derived by using the automatic parameters generation procedure available in Kong et al. (2018)'s model.

2.2.3 EOSs for explosive, water, and air

The widely used EOS, the Jones–Wilkins–Lee (JWL) equation (Hallquist, 2006), was used to model the pressure released by chemical energy during the explosion. The JWL EOS is defined as

$$P = A\left(1 - \frac{\omega}{R_1 V}\right)e^{-R_1 V} + B\left(1 - \frac{\omega}{R_2 V}\right)e^{-R_2 V} + \frac{\omega E_e}{V}, \quad (17)$$

where V denotes the relative volume of the detonation product, and E_e is the internal energy per unit volume of explosive. A, B, R_1, R_2, and ω are material parameters. The following parameters were adopted for the TNT explosive: explosive density ρ_e=1600 kg/m^3, A=3.712×10^{11} Pa, B=3.231×10^9 Pa, R_1=4.15, R_2=0.95, ω=0.3, and E_e=7.0×10^9 J/m^3.

Table 4 Parameters of the concrete

Parameter	Value
Compressive strength, f_c (MPa)	14.9
Tensile strength, T (MPa)	1.46
Elastic modulus, E (GPa)	20.1
Poisson's ratio, v	0.2
Strength parameter, a_1	0.58
Strength parameter, a_2 (MPa^{-1})	1.68×10^{-3}
Damage constant, d_1	0.042
Damage constant, d_2	1.53
Softening constant, τ	1.0
Fracture strain, ε_{frac}	0.015
Parameters of EOS	Refer to Kong et al. (2018)

The Gruneisen EOS (Hallquist, 2006) was adopted to calculate the internal characteristics of water, with its form determined by the state of the water. The Gruneisen EOS with cubic wave velocity–particle velocity defines the pressure for compressive material as follows:

$$P = \frac{\rho_0 C^2 \mu \left[1 + \left(1 - \frac{\kappa_0}{2}\right)\mu - \frac{\alpha_w}{2}\mu^2\right]}{1 - (S_1 - 1)\mu - S_2 \frac{\mu^2}{\mu+1} - S_3 \frac{\mu^3}{(\mu+1)^2}} + (\kappa_0 + \alpha_w \mu) E_w, \quad (18)$$

where E_w is the internal energy per unit volume of water, and C denotes the intercept of the wave velocity–particle velocity curve. S_1, S_2, and S_3 are coefficients of the slope of the wave velocity–particle velocity curve. ρ_0 represents the initial density of water. κ_0 is the Gruneisen gamma, and α_w is the first-order volume correction to κ_0. The selected values of each parameter were: ρ_0=1000 kg/m^3, C=1480 m/s,

S_1=2.56, S_2=1.986, S_3=1.2268, κ_0=0.35, E_w=1.89×10^6 J/m^3, and α_w=0.

The linear polynomial EOS (Hallquist, 2006) was adopted to describe the volumetric behavior of the air. The pressure was defined as

$$P = C_0 + C_1\mu + C_2\mu^2 + C_3\mu^3 + (C_4 + C_5\mu + C_6\mu^2)E_a, \tag{19}$$

where E_a represents the internal energy per unit volume of air. For ideal gases, the coefficients widely used in Eq. (19) are C_0=C_1=C_2=C_3=C_6=0 and C_4=C_5=0.401. The air mass density ρ_a was 1.293 kg/m^3 and the initial energy E_a was 2.5×10^5 J/m^3.

3 Results and discussion

A comparative analysis of the results of the centrifuge test UE-04 and numerical simulations is presented in this section. The underlying mechanism for the observed dam failures is also discussed. Some of the dam failures produced during historical wars are summarized and found to share failure modes similar to that found in this study.

3.1 Dam failures

First, to gain an insight into the tensile damage process of a concrete gravity dam subjected to a near-field UNDEX, the numerically predicted tensile damage evolution profiles are illustrated in Fig. 8. The tensile damage profile at a time of 2.0 ms is considered as the final state, as no differences could be observed afterwards. According to Fig. 8, the tensile damage evolution associated with the probable underlying physical process can be presented as follows. First, a compressive stress wave is generated when the shock wave produced by an UNDEX arrives at the upstream face of the dam. Therefore, the upstream face is initially under a state of compression. Since the upper part is very thin, the compressive stress wave could quickly reach the downstream face. The reflection of the compressive stress wave would induce a tensile stress wave in the downstream face. Tensile damage then first appears in the downstream face, as shown in Fig. 8a at 0.05 ms. After that, tensile damage occurs in the upstream face at 0.10 ms (Fig. 8b). It develops rapidly, and finally covers all the upstream face at 0.35 ms (Fig. 8d), and is induced mainly by bending. Specifically, for a concrete gravity dam with great mass, the dam bottom is
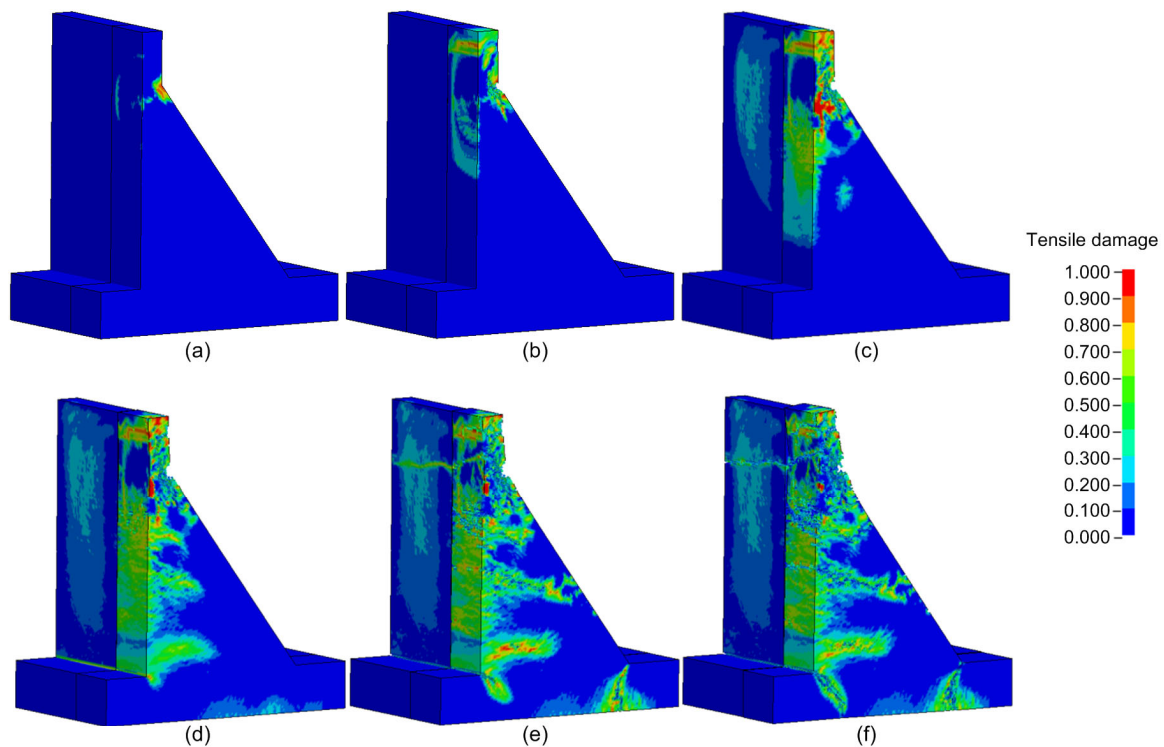

Fig. 8 Numerically predicted tensile damage evolution: (a) 0.05 ms; (b) 0.10 ms; (c) 0.20 ms; (d) 0.35 ms; (e) 0.60 ms; (f) 2.0 ms

internally fixed, which is similar to a cantilever beam with different section areas. In this context, as the shock wave arrives at the top and the bottom of the upstream face, the generated bending moments would force the dam to bend in the downstream direction. In this situation, the downstream face is under compression, while the whole upstream face is under tension. After the tensile damage covers the whole upstream face, three major tensile damage areas inside the dam, i.e. the upper part, the lower part, and the dam bottom near the foundation, could be observed at 0.60 ms (Fig. 8e). The tensile damage in the lower part of the dam initiates from the upstream face and develops in the downstream direction.

Fig. 9 shows a comparison of the damaged dam between the centrifuge test UE-04 and numerical simulations. The dam failures observed in the upstream face and the downstream face of the centrifuge test UE-04 are presented in Fig. 10, as supplements for Fig. 9b. According to the observations, two tensile fractures inside the dam are striking, one in the upper part and the other in the lower part. The fracture in the upper part is at the change in the downstream slope, and is normal to the upstream face. In addition to the severe tensile damage in the upstream face induced by bending tensile loads, severe tensile damage in the upper part of the downstream face could also be observed (Fig. 9a right and Fig. 10b). With a relatively small section area there, the compressive stress wave generated in the upstream face could quickly reach the downstream face with little attenuation. Reflection of this compressive stress wave then induces a tensile stress wave of high intensity, which is responsible for the severe tensile

damage in the downstream face. Hence, for the fracture in the upper part, the effects of the bending tension from the upstream face and the reflected tensile stress wave in the downstream face are coupled. This will be further proved in Section 3.2 using the recorded strain histories.

The second fracture is in the lower part at around one third of the height of the dam. This fracture is no longer normal to the upstream face, as there is a horizontal angle with a measured value of about 15°. Driven by the bending tensile loads, the second fracture develops from the upstream face in the downstream direction, penetrating through the dam body. Owing to the large section area of the dam body, there is strong attenuation of the compressive stress wave as it propagates from upstream to downstream. In this context, the tensile stress wave reflected by the compressive stress wave at the lower part of the downstream face is relatively weak. Thus, the second fracture in the lower part is produced mainly by the bending tensile stress. This will be further confirmed by the recorded strain histories
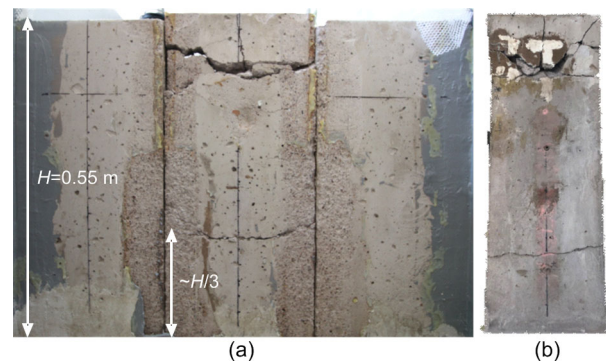

(a)   (b)

Fig. 10 Dam failures from the centrifuge test UE-04: (a) upstream face; (b) downstream face
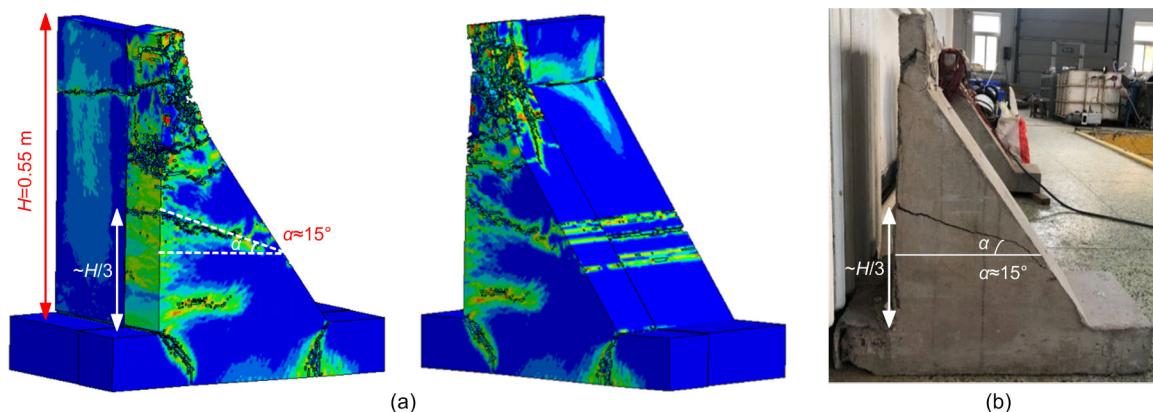

(a)   (b)

Fig. 9 Dam failures from numerical simulations (a) and centrifuge test UE-04 (b) (α: horizontal angle of the fracture)

below. Note that the main features of the tensile fractures, including their position and direction of fracture, were nearly identical for the centrifuge test UE-04 and the numerical simulations.

However, the numerically predicted dam failures were more severe than those from the centrifuge tests. For example, Fig. 10 shows that no fracture could be observed in the two side dam blocks following the centrifuge test, which is inconsistent with the tensile fracture in the upper part for both the middle and the side dam blocks for the numerical predictions (Fig. 9a left). This may be attributed to the presence of free water in the concrete greatly enhancing the tensile strength of concrete under high-strain-rate conditions (Ross et al., 1996; Cadoni et al., 2001; Zheng and Li, 2004; Erzar and Forquin, 2011; Huang et al., 2020a, 2020b). Generally, for strain rates ranging from 10^{-5} to 10^2 s^{-1}, the tensile strength of saturated concrete is 1 to 2 times that of dry concrete. Note that free water not only affects the tensile strength of concrete, but also influences the deviatoric strength and volumetric stiffness of concrete, with much lower deviatoric strength capacity and higher volumetric stiffness for saturated concrete than dry concrete. However, the tensile fractures considered in this study for a concrete gravity dam subjected to UNDEX, are governed mainly by the tensile behaviors of concrete dams. The deviatoric behaviors under a stress state of triaxial compression and the volumetric behaviors under hydrostatic pressure of concrete have limited effects on the tensile fractures concerned here (Huang et al., 2020a). For a concrete dam surrounded by water, such as the concrete dam used in the centrifuge tests, the concrete is internally totally or partly saturated. Thus, the free water effect acts on the concrete dam in the centrifuge tests. However, the free water effect is currently not considered in the model proposed by Kong et al. (2018). For a concrete model without consideration of the free water effect, the numerical predictions will overestimate the tensile damage to saturated concretes. In addition, the waterproof treatment applied on the surfaces between the three dam blocks, and the surfaces between the dam blocks and container walls (Fig. 1b), may also partly strengthen the concrete dams used in the centrifuge tests. This waterproof treatment, therefore, may have also contributed to the gap between the centrifuge

test results and numerical predictions.

Furthermore, numerical simulations predict the occurrence of obvious tensile damage at the dam heel near the foundation, but no visible cracks were found in the centrifuge test. One of the probable reasons could be the reinforcement of the foundation caused by the pouring of a layer of waterproof cement on the foundation in the centrifuge tests (Fig. 1b).

3.2 Strain histories

The recorded *z*-strain histories of the upstream and downstream faces provide strong evidence for the underlying mechanism of the dam failures observed in the centrifuge tests and numerical simulations. Several representative positions in the upstream face and downstream face are marked in Fig. 11. The *z*-strain histories of positions in the upstream face are depicted in Fig. 12, while those in the downstream face are presented in Fig. 13. In this study, negative values of strain denote compression.
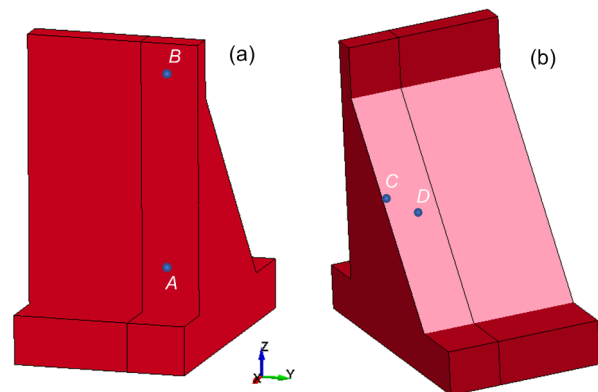

Fig. 11 Several representative positions in the upstream face (a) and downstream face (b) of the dam

From Fig. 12, a similar tendency can be observed for the *z*-strain histories of position *A* in the lower part and position *B* in the upper part of the upstream face. The strain histories begin with a short stage of compression, and then transform into a state of tension. This is consistent with the analysis above: namely, as the shock wave reaches the dam, the upstream face is first under a state of compression; subsequently, bending moments force the dam to bend towards the downstream, putting the upstream face under tension. Note the release of tension at intervals, which is reflected in a sharp decline of the tensile strain (Fig. 12). This is due mainly to the
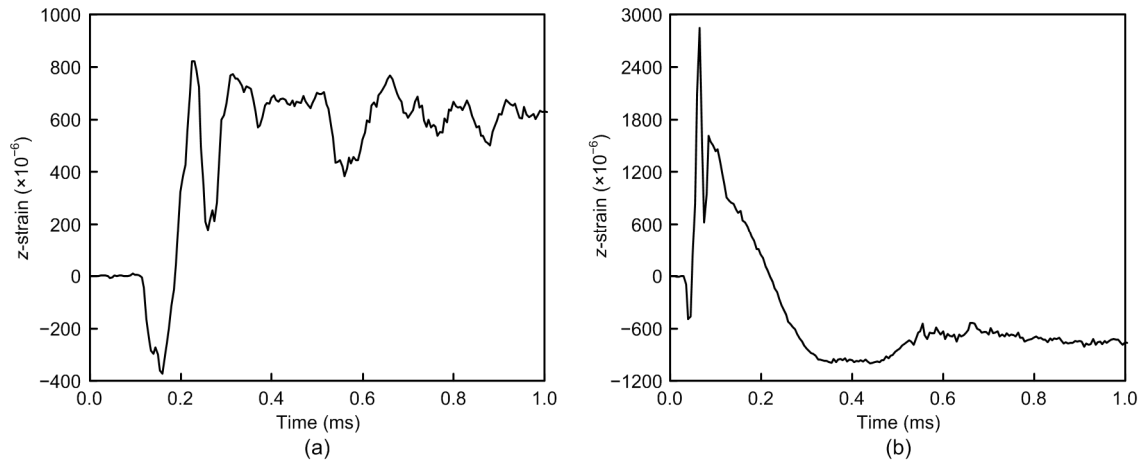
Fig. 12 Numerical predictions of *z*-strain histories of positions in the upstream face: (a) position *A* in the lower part; (b) position *B* in the upper part (negative value denotes compression)
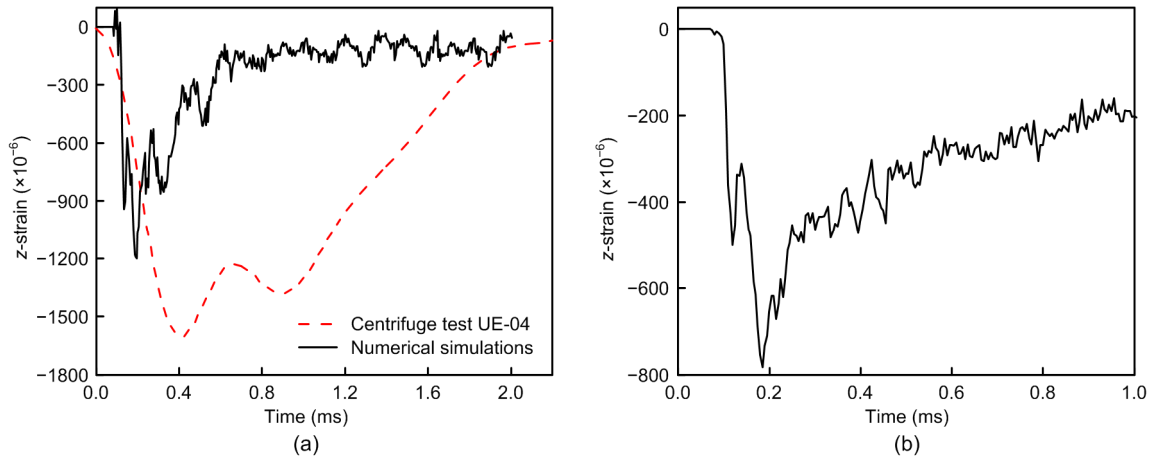

Fig. 13 *z*-strain histories of positions in the downstream face: (a) position *C*; (b) position *D* (negative value denotes compression)

reflected tensile stress wave on the downstream face, which intermittently forces the dam to bend towards the upstream (that is why some tensile cracks appear in the downstream face), resulting in the release of tension in the upstream face. After the short stage of compression, position *A* in the lower part of the upstream face is under a state of tension all the time, despite the release of tension at intervals contributed by the reflected tensile stress wave. This observation supports the conclusion that the second fracture in the lower part is produced mainly by bending tensile loads from the upstream face. However, the case of position *B* in the upper part of the upstream face is different. After the short stage of compression (induced by the compressive stress wave), position *B* is first under a state of tension. During this stage, the

tensile strain is very large, which reveals the severe tensile damage induced by the bending tensile loads from the upstream face. However, after that, the upstream face is again under a state of compression. This stage of compression is produced by the reflected tensile stress wave in the downstream face, as discussed above. This variation in the strain history of position *B* confirms the existence of the coupled effects of the fracture in the upper part, as mentioned in Section 3.1.

According to the underlying mechanism of the fracture in the lower part, the upstream face is under tension induced by the bending tensile loads. Accordingly, the downstream face should be under a state of compression. The strain histories of positions *C* and *D* in the lower part of the downstream face are

depicted in Fig. 13. Clearly, both positions are under the state of compression all the time. The *z*-strain history of position *C* from centrifuge test UE-04 is also presented in Fig. 13a, and coincides well with the numerical predictions.

3.3 Discussion

Consistent results from the centrifuge test UE-04 and numerical simulations have revealed the existence of two tensile fractures in a concrete gravity dam subjected to near-field UNDEX. The mechanism of the fracture could be ascribed to the effect of bending tensile failure. Fig. 14 presents the distribution of maximum tensile stresses predicted by numerical modeling along the height of the dam. Generally, two peaks exist in this tensile stress distribution, one in the upper part and the other in the lower part. The positions of the two peaks are consistent with those of the two tensile fractures (Figs. 9 and 10). The peaks in the upper part of the downstream and upstream faces are at the same altitude. The peak in the lower part of the downstream face is slightly lower than that in the upstream face, which is consistent with the horizontal angle of the fracture. From this point of view, predicting the tensile stress distribution along the height of a concrete gravity dam in response to UNDEX is an alternative way to predict the positions of the tensile fractures.

A breach of the dam will probably occur if the UNDEX is severe enough or if the dam suffers from another explosion with the existence of previously produced tensile fractures inside the dam. Fig. 15 schematically illustrates the modes of dam breach that might be observed, based on the results of the dam failures from the centrifuge test and numerical simulations. Associated with the tensile fracture in the upper part, a shallow breach is possible in the upper part of the dam (Fig. 15a). If there is another tensile fracture in the lower part of the dam, the breach will be deeper, depending on the position of this fracture. In the case of the configuration of the dam model in this study, i.e. large amounts of explosives detonated near the upstream face, a deep breach associated with the second fracture may be observed (Fig. 15b). Realistic dam failures suffered by a dam prototype following a near-field UNDEX are hardly accessible. Nevertheless, dam structures are prime targets during wars, and a number of dams have been attacked in military history. Some were attacked using large amounts of explosives which were detonated near or in contact with the dams (Wang et al., 2020). Fig. 16 presents some dam failures produced by military attacks in history (Wang et al., 2020). Generally, these dam failures share a similar mode, namely a breach of variable width and depth in the upper part. For example, the Möhne dam was 40 m high, with a 6.25-m crest width and 34-m base width, and was hit by two tombs in the center of the upstream face. The condition of the Möhne dam was very similar to the configuration of the dam prototype used in this study (dam height 44 m, crest width 4 m, and base width 30 m, according to the scaling law for UNDEX in the centrifuge, Fig. 2). The results are encouraging: the failure of this dam with a deep breach (Fig. 16) was
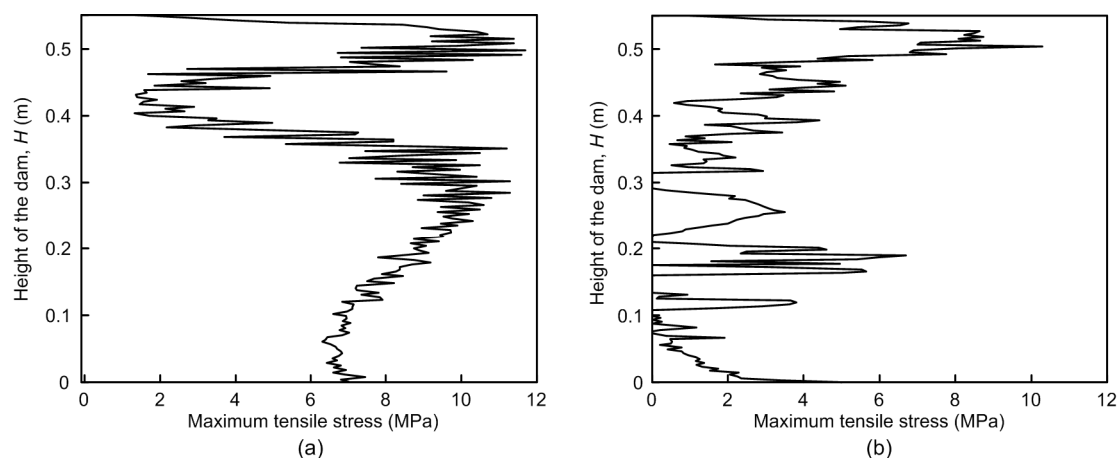

Fig. 14 Numerically predicted maximum tensile stresses along the height of the dam: (a) upstream face; (b) downstream face
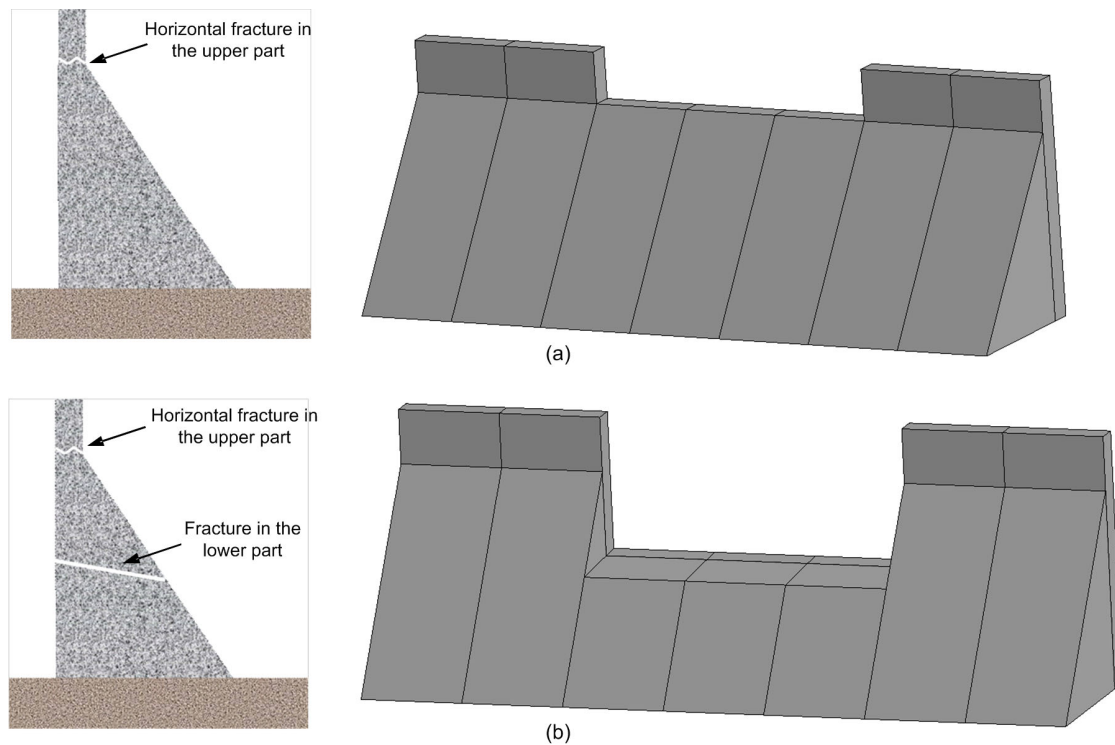
Fig. 15 Schematic dam failures based on the results in this study: (a) a shallow breach; (b) a deep breach
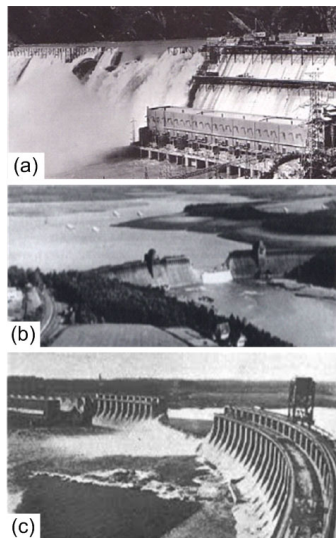

Fig. 16 Dam failures due to military attacks in history: (a) Suiho dam, Korean war, 1952; (b) Möhne dam, Second World War, 1943; (c) Dnjeprostroj dam, Second World War, 1941

consistent with the results presented in this study. In this context, determination of the position of the tensile fracture in the lower part is essential, as it internally determines the depth of the breach for a dam subjected to UNDEX.

4 Conclusions

Centrifuge tests and numerical simulations were performed in this study to investigate the failure of a concrete gravity dam subjected to a near-field underwater explosion. Results of the centrifuge tests and numerical simulations were in good agreement. There were two tensile fractures inside the dam: one in the upper part and the other in the lower part of the dam. The mechanism of the dam failure could be reasonably explained by a failure mode induced by bending tension. Our conclusions can be summarized as follows:

1. The thin upper part of a concrete gravity dam is vulnerable. A horizontal tensile fracture was observed at the break of the downstream slope. This fracture resulted from the coupled effects of the bending tensile stress in the upstream face and the reflected tensile stress wave in the downstream face.

2. A tensile fracture was also observed in the lower part at around one third of the height of the dam, and at a horizontal angle of about 15°. This fracture was produced mainly by the bending tensile stress in the upstream face, causing the fracture to propagate in

a downstream direction. Recorded strain histories provided strong evidence for the underlying mechanism associated with the two tensile fractures.

3. Some dam failures produced in historical wars shared a similar failure mode, generally a breach of variable depth in the upper part of the dam. This failure mode is consistent with the results presented in this study. The position of the tensile fracture in the lower part internally determines the depth of the breach for a dam subjected to underwater explosion.

Contributors

Xie-ping HUANG performed the numerical simulations, analyzed and validated the centrifugal test data, wrote the first draft of the manuscript, and revised and edited the final version. Jing HU designed the centrifuge tests and participated in the revisions of the manuscript. Xue-dong ZHANG and Zi-tao ZHANG participated in the design of the centrifuge tests. Xiang-zhen KONG helped to perform the numerical simulations.

Conflict of interest

Xie-ping HUANG, Jing HU, Xue-dong ZHANG, Zi-tao ZHANG, and Xiang-zhen KONG declare that they have no conflict of interest.

References

Benson DJ, 1992. Computational methods in Lagrangian and Eulerian hydrocodes. *Computer Methods in Applied Mechanics and Engineering*, 99(2-3):235-394.
https://doi.org/10.1016/0045-7825(92)90042-I

Cadoni E, Labibes K, Berra M, et al., 2000. High-strain-rate tensile behaviour of concrete. *Magazine of Concrete Research*, 52(5):365-370.
https://doi.org/10.1680/macr.2000.52.5.365

Cadoni E, Labibes K, Albertini C, et al., 2001. Strain-rate effect on the tensile behaviour of concrete at different relative humidity levels. *Materials and Structures*, 34(1): 21-26.
https://doi.org/10.1007/BF02482196

Chen JY, Liu XP, Xu Q, 2017. Numerical simulation analysis of damage mode of concrete gravity dam under close-in explosion. *KSCE Journal of Civil Engineering*, 21(1): 397-407.
https://doi.org/10.1007/s12205-016-1082-4

Cole RH, Weller R, 1948. Underwater explosions. *Physics Today*, 1(6):35.
https://doi.org/10.1063/1.3066176

Erzar B, Forquin P, 2011. Free water influence on the dynamic tensile behaviour of concrete. *Applied Mechanics and Materials*, 82:45-50.
https://doi.org/10.4028/www.scientific.net/AMM.82.45

Hallquist JO, 2006. LS-DYNA Theory Manual. Lawrence Livermore National Laboratory, University of California, California, USA.

Hartmann T, Pietzsch A, Gebbeken N, 2010. A hydrocode material model for concrete. *International Journal of Protective Structures*, 1(4):443-468.
https://doi.org/10.1260/2041-4196.1.4.443

Hu J, Chen ZY, Zhang XD, et al., 2017. Underwater explosion in centrifuge part I: validation and calibration of scaling laws. *Science China Technological Sciences*, 60(11): 1638-1657.
https://doi.org/10.1007/s11431-017-9083-0

Hu J, Chen ZY, Zhang XD, et al., 2020a. Investigation of a new shock factor to assess an air-backed structure subjected to a spherical wave caused by an underwater explosion. *Journal of Structural Engineering*, 146(10): 04020220.
https://doi.org/10.1061/(ASCE)ST.1943-541X.0002788

Hu J, Chen ZY, Zhang XD, et al., 2020b. Modeling bubble motions by underwater explosion in a centrifuge. *Journal of Fluids Engineering*, 142(4):041401.
https://doi.org/10.1115/1.4045435

Huang XP, Kong XZ, Hu J, et al., 2020a. The influence of free water content on ballistic performances of concrete targets. *International Journal of Impact Engineering*, 139: 103530.
https://doi.org/10.1016/j.ijimpeng.2020.103530

Huang XP, Kong XZ, Chen ZY, et al., 2020b. Equation of state for saturated concrete: a mesoscopic study. *International Journal of Impact Engineering*, 144:103669.
https://doi.org/10.1016/j.ijimpeng.2020.103669

Huang XP, Kong XZ, Chen ZY, et al., 2020c. A computational constitutive model for rock in hydrocode. *International Journal of Impact Engineering*, 145:103687.
https://doi.org/10.1016/j.ijimpeng.2020.103687

Kalateh F, 2019. Dynamic failure analysis of concrete dams under air blast using coupled Euler-Lagrange finite element method. *Frontiers of Structural and Civil Engineering*, 13(1):15-37.
https://doi.org/10.1007/s11709-018-0465-7

Kong XZ, Fang Q, Chen L, et al., 2018. A new material model for concrete subjected to intense dynamic loadings. *International Journal of Impact Engineering*, 120:60-78.
https://doi.org/10.1016/j.ijimpeng.2018.05.006

Li Q, Wang GH, Lu WB, et al., 2018. Failure modes and effect analysis of concrete gravity dams subjected to underwater contact explosion considering the hydrostatic pressure. *Engineering Failure Analysis*, 85:62-76.
https://doi.org/10.1016/j.engfailanal.2017.12.008

Lu L, Li X, Zhou J, 2014. Study of damage to a high concrete dam subjected to underwater shock waves. *Earthquake Engineering and Engineering Vibration*, 13(2):337-346.
https://doi.org/10.1007/s11803-014-0235-z

Lu L, Li X, Zhou J, et al., 2016. Numerical simulation of shock response and dynamic fracture of a concrete dam subjected to impact load. *Earth Sciences Research Journal*, 20(1):M1-M6.

https://doi.org/10.15446/esrj.v20n1.54133

Rajendran R, Lee JM, 2009. Blast loaded plates. *Marine Structures*, 22(2):99-127.
https://doi.org/10.1016/j.marstruc.2008.04.001

Ren XD, Shao Y, 2019. Numerical investigation on damage of concrete gravity dam during noncontact underwater explosion. *Journal of Performance of Constructed Facilities*, 33(6):04019066.
https://doi.org/10.1061/(ASCE)CF.1943-5509.0001332

Ross CA, Jerome DM, Tedesco JW, et al., 1996. Moisture and strain rate effects on concrete strength. *ACI Materials Journal*, 93(3):293-300.
https://doi.org/10.14359/9814

Saadatfar S, Zahmatkesh A, 2018. Evaluation of underwater blast on concrete gravity dams using three-dimensional finite-element model. *AUT Journal of Civil Engineering*, 2(1):69-78.
https://doi.org/10.22060/AJCE.2018.13467.5416

Schuler H, Mayrhofer C, Thoma K, 2006. Spall experiments for the measurement of the tensile strength and fracture energy of concrete at high strain rates. *International Journal of Impact Engineering*, 32(10):1635-1650.
https://doi.org/10.1016/j.ijimpeng.2005.01.010

Snay HG, 1962. Underwater Explosion Phenomena: the Parameters of Migrating Bubbles. Technical Report NAVORD 4185, Naval Ordnance Laboratory, White Oak, USA.

Snay HG, Tipton RV, 1963. Charts for the Parameters of Migrating Explosion Bubbles. NOLTR Report 62-184, Naval Ordnance Laboratory, White Oak, USA.

Swisdak Jr MM, 1978. Explosion Effects and Properties: Part II–Explosion Effects in Water. NSWC/WOL TR 76-116, Naval Surface Weapons Center, Silver Spring, USA.

Vanadit-Ellis W, Davis LK, 2010. Physical modeling of concrete gravity dam vulnerability to explosions. Proceedings of the 2010 International WaterSide Security Conference, p.1-11.
https://doi.org/10.1109/WSSC.2010.5730291

Wang GH, Zhang SR, 2014. Damage prediction of concrete gravity dams subjected to underwater explosion shock loading. *Engineering Failure Analysis*, 39:72-91.
https://doi.org/10.1016/j.engfailanal.2014.01.018

Wang GH, Lu WB, Yang GD, et al., 2020. A state-of-the-art review on blast resistance and protection of high dams to blast loads. *International Journal of Impact Engineering*, 139:103529.
https://doi.org/10.1016/j.ijimpeng.2020.103529

Xu H, Wen HM, 2013. Semi-empirical equations for the dynamic strength enhancement of concrete-like materials. *International Journal of Impact Engineering*, 60:76-81.
https://doi.org/10.1016/j.ijimpeng.2013.04.005

Xu Q, Chen JY, Li J, et al., 2013. Coupled elasto-plasticity damage constitutive models for concrete. *Journal of Zhejiang University-SCIENCE A (Applied Physics & Engineering)*, 14(4):256-267.
https://doi.org/10.1631/jzus.A1200196

Yan DM, Lin G, 2006. Dynamic properties of concrete in direct tension. *Cement and Concrete Research*, 36(7):1371-1378.
https://doi.org/10.1016/j.cemconres.2006.03.003

Yang GD, Wang GH, Lu WB, et al., 2018. A SPH-Lagrangian-Eulerian approach for the simulation of concrete gravity dams under combined effects of penetration and explosion. *KSCE Journal of Civil Engineering*, 22(8):3085-3101.
https://doi.org/10.1007/s12205-017-0610-1

Zhang SR, Wang GH, Wang C, et al., 2014. Numerical simulation of failure modes of concrete gravity dams subjected to underwater explosion. *Engineering Failure Analysis*, 36:49-64.
https://doi.org/10.1016/j.engfailanal.2013.10.001

Zheng D, Li QB, 2004. An explanation for rate effect of concrete strength based on fracture toughness including free water viscosity. *Engineering Fracture Mechanics*, 71(16-17):2319-2327.
https://doi.org/10.1016/j.engfracmech.2004.01.012

中文概要

题　目： 混凝土重力坝水下爆炸荷载作用下的弯曲破坏

目　的： 探索混凝土重力坝在水下爆炸荷载作用下的破坏模式和破坏机理。

方　法： 1. 利用离心机试验和数值模拟对混凝土重力坝在水下爆炸荷载下的破坏模式进行对比研究；2. 结合水下爆炸的物理过程，对大坝破坏模式的产生机理进行分析，并利用应变历史对其进行验证。

结　论： 1. 混凝土重力坝较薄的上部易受破坏，且在下游拐角位置可以观察到水平断裂。2. 在大坝下部约1/3位置处，可观察到另一拉伸断裂；该断裂主要受上游面的弯曲拉应力控制，使该断裂向下游发展。3. 一些在历史战争中产生的大坝破坏具有相似的破坏模式，即通常在大坝上部出现不同深度的溃口；这种失效模式与本研究的结果一致。4. 坝体下部拉伸断裂的位置决定了溃口的深度。

关键词： 离心机试验；数值模拟；混凝土重力坝；水下爆炸；弯曲破坏